



저작자표시-비영리-변경금지 2.0 대한민국

이용자는 아래의 조건을 따르는 경우에 한하여 자유롭게

- 이 저작물을 복제, 배포, 전송, 전시, 공연 및 방송할 수 있습니다.

다음과 같은 조건을 따라야 합니다:



저작자표시. 귀하는 원저작자를 표시하여야 합니다.



비영리. 귀하는 이 저작물을 영리 목적으로 이용할 수 없습니다.



변경금지. 귀하는 이 저작물을 개작, 변형 또는 가공할 수 없습니다.

- 귀하는, 이 저작물의 재이용이나 배포의 경우, 이 저작물에 적용된 이용허락조건을 명확하게 나타내어야 합니다.
- 저작권자로부터 별도의 허가를 받으면 이러한 조건들은 적용되지 않습니다.

저작권법에 따른 이용자의 권리는 위의 내용에 의하여 영향을 받지 않습니다.

이것은 [이용허락규약\(Legal Code\)](#)을 이해하기 쉽게 요약한 것입니다.

[Disclaimer](#)

Thesis for the M.S Degree

**Detection of Submarine Groundwater
Discharge (SGD) Signal by Stacking
Landsat Thermal Infrared (TIR)
Images in Jeju Island**

**Landsat 열적외선 영상의 중첩을 통한
제주도에서의 SGD 신호 탐지**

February, 2018

**Graduate School of
Earth and Environmental Sciences
Seoul National University**

Yunjee Kim

Abstract

Although submarine groundwater discharge (SGD) has recently attracted, dispersive and weak SGD signals have not been satisfactorily identified. Since SGD varies spatially and temporally, the locations of SGD are generally hard to detect from a single satellite image. Due to such spatiotemporal characteristics, multi temporal data are required to detect SGD appeared in various patterns and weak amplitudes. Additionally, weak SGD signals may be missed on a single satellite image as they may fall below the noise threshold dictated by Landsat's noise equivalent differential temperature (NEdT). Thus, this study proposes a practical method by applying stacking method to Landsat data for SGD detection.

The stacking method is comprised of two main processing steps: 1) mask out the land area and calculate sea surface temperature (SST) anomalies by subtracting the offshore SST, and 2) stack SST anomalies by summing multiple images. The optimal seasonal and tidal conditions for the detection of a weak SGD signal were determined, and then Landsat images satisfying the conditions of month and tide level were stacked in order to strengthen SGD signals and confirm the presence of SGD.

In this study, the method was applied to three sites on Jeju Island. The results show that this method is very successful at detecting SGD signal, even for weak signals.

Keywords : Thermal infrared(TIR) remote sensing, Landsat, Submarine groundwater discharge (SGD), Stacking, Noise equivalent differential temperature (NEdT)

Student Number : 2016-20410

Contents Table

1. Introduction.....	1
2. Methodology.....	4
2.1 Theoretical Basis of TIR Remote Sensing and Stacking.....	4
2.1.1 TIR Remote Sensing in SGD Detection.....	4
2.1.2 Atmospheric Correction.....	5
2.1.3 Conversion of DN to SST.....	6
2.1.4 SST Anomaly Estimation.....	10
2.1.5 Stacking Method.....	11
2.2. Study Area and Dataset.....	12
2.2.1 Study Area.....	12
2.2.2 Landsat Data.....	15
2.2.3 Airborne Data.....	18
2.2.4 Comparison between Airborne Data and Landsat Data.....	18
2.3 Data Processing.....	21
3. Stacking Condition Analysis.....	24
3.1 Spatial and Temporal Variability of SGD.....	24
3.2 Relationship between SST and SST Anomaly.....	28
3.3 Monthly Analysis of SST Anomaly.....	30
3.4 Tidal Analysis of SST Anomaly.....	33
3.5 Stacking Condition Analysis with NEdT.....	36
4. Stacking Landsat Data Satisfying the Optimum Condition.....	40
4.1 Stacking Under the Optimum Condition.....	40

4.2 Validation with Airborne Data.....	45
5. Conclusion.....	47
References.....	49
국문 요약.....	56

Figure List

- Figure 1. Map of Jeju Island showing the locations of the study sites. (a) Samyang Black Sand Beach, (b) Sinsan-ri Dock, and (c) Oedolgae Rock. The tide stations and meteorological stations on Jeju Island are showed by red triangles and blue circles, respectively.....14
- Figure 2. Flow chart for the stacking processes. The gray boxes and white boxes are essential and additional process to detect faint SGD signals, respectively.....23
- Figure 3. Landsat TIR images at each date in Samyang Black Sand Beach. L5, L7 and L8 refer to Landsat_5, Landsat_7 and Landsat_8, respectively. The spatial resolutions of the TIR band of the Landsat satellites are 120 m, 60 m, and 100 m for L5, L7, and L8, respectively.....25
- Figure 4. Landsat TIR images at each date in Sinsan-ri Dock. L5, L7 and L8 refer to Landsat_5, Landsat_7 and Landsat_8, respectively. The spatial resolutions of the TIR band of the Landsat satellites are 120 m, 60 m, and 100 m for L5, L7, and L8, respectively.....26
- Figure 5. Landsat TIR images at each date in Oedolgae Rock. L5, L7 and L8 refer to Landsat_5, Landsat_7 and Landsat_8, respectively. The spatial resolutions of the TIR band of the Landsat satellites are 120 m, 60 m, and 100 m for L5, L7, and L8, respectively.....27

Figure 6. SST anomalies as a function of SST at each site. (a) Samyang Black Sand Beach, (b) Sinsan-ri Dock, and (c) Oedolgae Rock.....29

Figure 7. SST anomalies according to month of year at each site. (a) Samyang Black Sand Beach, (b) Sinsan-ri Dock, and (c) Oedolgae Rock..32

Figure 8. SST anomalies according to tide level (H: High, HL: High to Low(midebbing), L: Low, LH: Low to High(midrising)) between June and September at each site. (a) Samyang Black Sand Beach, (b) Sinsan-ri Dock, and (c) Oedolgae Rock.....35

Figure 9. Average SST anomaly for three different stacking conditions as well as all the data. The conditions used to define the stacking conditions are described in Table 3. The red line shows the NEdT of the Landsat data.....38

Figure 10. Images of stacked SST anomalies corresponding to each conditions at Samyang Black Sand Beach. (a) Summer condition (b) Low tide in summer condition.....42

Figure 11. Images of stacked SST anomalies corresponding to each conditions at Sinsan-ri Dock. (a) Summer condition (b) Low tide in summer condition.....43

Figure 12. Images of stacked SST anomalies corresponding to each conditions at Oedolgae Rock. (a) Summer condition (b) Low tide in summer condition.....44

Figure 13. Airborne TIR images acquired at low tide on August 5, 2015 at each study sites. (a) Samyang Black Sand Beach, (b) Sinsan-ri Dock, and (c) Oedolgae Rock.....46

Table List

Table 1. The values of parameters necessary for the temperature calculation.....	9
Table 2. List of satellite images used in this study. The data acquisition dates and tidal conditions at the study sites.....	17
Table 3. Comparison between airborne data and Landsat data.....	20
Table 4. The averages SST anomalies for the four stacking conditions. Number of data refers to the number of images fulfilling each condition...	39

1. Introduction

Submarine groundwater discharge (SGD) is a common oceanographic phenomenon which has become extensively known as a key role in transmission between coastal aquifers and ocean [Moore, 1999; Peterson et al., 2009]. SGD has considerable impacts on the geochemistry, geobiology, oceanography and hydrology of the coastal environment [Moore, 2010]. Since SGD plays a role as a direct path between land and ocean, it can alter the chemical composition of aquifers as well as sending chemical materials such as minerals, nutrients, and carbon to the ocean [Beck et al., 2007; Cyronak et al., 2014; Knee & Paytan, 2011; Moore, 2010]. Transport of nutrients can cause harmful algal blooms [Gobler & Sanudo-Wilhelmy, 2001; LaRoche et al., 1997; Paerl, 1997]. SGD also transports man-made materials like sewage and soluble refuse could also cause contamination of coastal environment [Burnett et al., 2001].

Although SGD can have negative impacts on coastal environments, SGD may provide part of the solution to the problem of future water scarcity [Xing et al., 2014]. Since fresh submarine groundwater discharge (FSGD) has low salinity, it can be a valuable source of water supply.

In many previous studies, airborne thermal infrared (TIR) images, radium isotopes (^{223}Ra , ^{224}Ra , ^{226}Ra , and ^{228}Ra), and radon (^{222}Rn) were prevalently used to detect and measure flux of SGD [Kelly et al., 2013; Lee et al., 2016; Mejías et al., 2012; Peterson et al., 2009; Tamborski et al., 2015]. Since airborne platforms provide high spatial resolution data, airborne TIR images

have been used increasingly for SGD detection. Although high resolution airborne TIR images play an integral role in SGD identification, they can only offer a snapshot of SGD outflows [Mallast et al., 2013]. Since the appearance of SGD varies spatially and temporally, it can be challenging to identify discharge locations [Kelly et al., 2013; Mallast et al., 2013; Wilson & Rocha, 2012]. Therefore, usage of multi-temporal data is a quite good way to distinguish various patterns which vary in time [Mallast et al., 2013]. Although airborne TIR can acquire data at high spatial resolutions, the collection of multi-temporal data can be difficult due to several factors such as weather conditions and mechanical problems. Because of these factors, multi-temporal data are more easily acquired from satellites than airborne platforms. Despite the clear advantages of satellite TIR data, not many studies have accomplished to detect SGD signals using satellite TIR data [Al Bassam et al., 2013; Becker et al., 2006; Park & Yoon, 2013; Tamborski et al., 2015; Tcherepanov et al., 2005; Varma et al., 2010; Wang et al., 2008; Wilson & Rocha, 2012]. Tamborski (2015) compared the resolutions of airborne and space-borne TIR image in order to know minimum resolution of thermal image through a quantitative analysis. In Long Island, TIR images need to have a minimum spatial resolution of 30 m, and a 15 m resolution was needed for a quantitative analysis [Tamborski et al., 2015].

Park and Yoon (2013) used the same potential SGD temperature range (16 – 18 °C) for all data in Jeju Island, and then, extracted and overlapped the data corresponding to that range from three Landsat TIR images. Since the appearance of SGD in Landsat TIR images is affected by sea surface temperature (SST), it can be showed at differently depending on time.

Furthermore, if absolute temperature is used, some of the data within the range may not result from SGD but will mistakenly be considered SGD signal. Therefore, I used SST anomalies instead of absolute temperatures to detect SGD signal.

This study presents an improved method of SGD signal detection using stacking TIR images. The primary objective of this study was to detection of SGD signal in Landsat data by applying a stacking method. The specific objectives were (1) to detect weak SGD signals which are hardly identifiable on a single satellite image, and (2) to find the optimal stacking conditions by analyzing SGD temperature characteristic as a function of the month and tide level.

2. Methodology

2.1. Theoretical Basis of TIR Remote Sensing and Stacking

2.1.1. TIR Remote Sensing in SGD detection

All objects which have above 0 K temperatures emit thermal energy, and TIR remote sensing utilizes that energy to identify temperature information. The thermal energy emitted from an object is transmitted to a TIR sensor through the air. In this process, some of thermal energy dissipates at particles in the air. Therefore, atmospheric correction is a process to determine the amount of energy emitted from an object by compensating the attenuation of the energy losses in the air.

SGD can be detected in TIR image due to its low temperature and low density. Due to its low salinity, SGD upwells when flows out from a SGD spring. Furthermore, since it has lower temperature than SST in the summer, SGD can be detected by TIR remote sensing, which responds to surface temperature.

2.1.2. Atmospheric Correction

In TIR remote sensing, atmospheric effect must be corrected for prior to further processing in order to derive accurate temperatures from thermal infrared energy. Skipping this step may cause a serious error in the calculated temperature. The temperatures calculated without the atmospheric correction are 5-10 K lower than the corrected value [Barsi et al., 2003].

Disregarding the any atmospheric phenomenon, the amount of radiation received at the sensor can be described as approximations of the radiative transfer equation (RTE):

$$L_{\lambda,sensor} = \tau_{\lambda} \cdot [\varepsilon_{\lambda} \cdot B_{\lambda}(T_{S_K}) + (1 - \varepsilon_{\lambda}) \cdot L_{\lambda,atm,\downarrow}] + L_{\lambda,atm,\uparrow} \quad (1)$$

where

$L_{\lambda,sensor}$ = at-sensor radiance [$W/(m^2 \cdot sr \cdot \mu m)$],

τ_{λ} = atmospheric transmittance,

T_{S_K} = surface temperature [K],

$B_{\lambda}(T_{S_K})$ = energy radiance at surface temperature [$W/(m^2 \cdot sr \cdot \mu m)$],

ε_{λ} = surface emissivity,

$L_{\lambda,atm,\downarrow}$ = downwelling atmospheric radiance [$W/(m^2 \cdot sr \cdot \mu m)$],

$L_{\lambda,atm,\uparrow}$ = upwelling atmospheric radiance [$W/(m^2 \cdot sr \cdot \mu m)$],

2.1.3. Conversion of DN to SST

The SST is computed according to the equation using spectral radiance at the surface. For Landsat 5 and 7 images, the equation to calculate $L_{\lambda,sensor}$ is

$$L_{\lambda,sensor} = [(L_{\lambda,max} - L_{\lambda,min}) / (Q_{c,max} - Q_{c,min})] \cdot (Q_c - Q_{c,min}) + L_{\lambda,min} \quad (2)$$

where

Q_c = the quantized calibrated pixel value in DN which represents raw data of Level 1 products [DN],

$Q_{c,max}$ = the maximum value of the quantized pixel corresponding to $L_{\lambda,max}$ [DN],

$Q_{c,min}$ = the minimum value of the quantized pixel corresponding to $L_{\lambda,min}$ [DN],

$L_{\lambda,max}$ = the spectral radiance at the sensor scaled to $Q_{c,max}$ [$W / (m^2 \cdot sr \cdot \mu m)$],

$L_{\lambda,min}$ = the spectral radiance at the sensor scaled to $Q_{c,min}$ [$W / (m^2 \cdot sr \cdot \mu m)$]

In the case of Landsat 8 images, the radiance at the aperture of the sensor is calculated using the following equation given by the U.S. Geological Survey (USGS):

$$L_{\lambda,sensor} = M_L \cdot Q_C + A_L \quad (3)$$

where

M_L = band-specific multiplicative rescaling factor,

A_L = band-specific additive rescaling factor

M_L , A_L are described as RADIANCE_MULT_BAND_10 or 11 and RADIANCE_ADD_BAND_10 or 11, respectively, in metadata.

After converting the DN to the spectral radiance at sensor ($L_{\lambda,sensor}$), the atmospheric correction for the spectral radiance at surface considered atmospheric correction is calculated following the equation (French et al., 2003):

$$L_{\lambda,surface} = [(L_{\lambda,sensor} - L_{\lambda,u})/\tau_{\lambda}] - (1 - \epsilon_{\lambda}) \cdot L_{\lambda,d} \quad (4)$$

To calculate $L_{\lambda,u}$, $L_{\lambda,d}$, and τ_{λ} , surface temperature and humidity information are required. Since land is masked, the SST data measured at several tide stations are considered as surface temperature. There are four tide stations and four meteorological stations at east, west, north, and south offshore Jeju Island (Fig. 1). Since the study sites are located north, east, and south of the Island, the data from each of the three meteorological and tide stations were used in this study. In specific, the surface temperature data were acquired from Jeju tide station in the north, Seongsanpo tide station in the east, and Seogwipo tide station in the south. Because Seongsanpo tide

station has only been operational since November 2003, only SST data were available at this station only after November 2003. Similar to the SST data, the humidity data were acquired from Jeju meteorological station in the north, Seongsan meteorological station in the east, and Seogwipo meteorological station in the south for radiance and transmittance calculation. The SST and humidity data were used from each of nearest metrological and tide stations for the atmospheric correction (Fig. 1). If the data were absent, averaging values at other sites have been used.

SST is calculated according to the equation [Chander & Helder, 2009; NASA] using $L_{\lambda,surface}$:

$$T_{S_C} = K_2 / \ln\left(\frac{K_1}{L_{\lambda,surface}} + 1\right) - 273 \quad (5)$$

where both K_1 , K_2 are calibration constants and T_{S_C} is surface temperature in Celsius. The constant values in eqs. (2), and (5) are given in Table 1, where Landsat 5, Landsat7 and Landsat8 mean band6, band6-1, and band10 values of corresponding Landsat, respectively. Since I only used single TIR band for both Landsat7 and Landsat8, only the parameter values of these bands were given.

Table 1. The values of parameters necessary for the temperature calculation [Chander & Helder, 2009; NASA].

	$L_{\lambda,min}$	$L_{\lambda,max}$	$Q_{c,min}$	$Q_{c,max}$	K_1	K_2
LANDSAT5	1.2378	15.3032		255	607.76	1260.56
LANDSAT7	0.0	17.04	1	255	666.09	1282.71
LANDSAT8	0.10033	22.0018		65535	774.89	1321.08

2.1.4. SST Anomaly Estimation

In this study, the SST anomaly refers to the temperature differences between the SGD temperature and offshore SST. The offshore SST is defined as SST data that contains only sea surface temperature data without any information of land or SGD.

The SST anomaly is calculated by

$$\Delta T = T_{\text{sea surface}} - T_{\text{offshore sea surface}} \quad (6)$$

where ΔT is SST anomaly, $T_{\text{sea surface}}$ means T_{S_C} which was calculated through the eqs. (1) - (6), $T_{\text{offshore sea surface}}$ is derived through nearest neighbor interpolation and extrapolation. Since the pixel values were not changed during the rearrangement process in this interpolation method, it was considered to be suitable for SGD detection which is highly important to catch extremely subtle temperature changes. For the sake of $T_{\text{offshore sea surface}}$ calculation, 10 percent of SST image pixels were arbitrarily selected. These pixels were selected in the sea where is around 400 m off from the coastal line to extract the SST that were hardly affected by land.

2.1.5. Stacking Method

The stacking method aims to detect subtle differences in temperature and magnify them to show up clearly. Even if there are some differences between SGD temperature and the SST, they may not be detectable in Landsat images due to the existence of their noise equivalent differential temperature (NEdT). NEdT, a minimum temperature difference that can be distinguished in a TIR image, provides information about the noise that can affect the actual signal [Redjimi, A et al., 2014]. Hence, differences in temperature smaller than NEdT are not detectable in Landsat TIR images. In specific, when the amount of outflowing SGD is small or even the amount is large but the outflow rate is low, the difference between SGD temperature and SST becomes small by mixing with seawater during upwelling.

In this study, SST anomalies derived in 2.1.2 through 2.1.4 were stacked together to detect SGD signals easily and efficiently.

2.2. Study Area and Dataset

2.2.1. Study Area

Jeju Island is a volcanic island located south southwest of the Korean peninsula (Figure 1). Jeju island is an elliptical island which is long in the horizontal direction and short in the vertical direction, with its axis running east-northeast to west-southwest direction [Kang et al., 2008]. Halla mountain, which has a height of 1950 m, is located in the central part of the island. The east and the west slopes are gentle in the foothills of this mountain, with steep slopes are in the north and the south. Over 360 cinder cones are evenly distributed across the island. This island is mainly composed of pyroclastic rocks formed by hydrovolcanism and volcanic rocks such as basalt, trachybasalt and trachyandesit. Since the lava flow which formed this island was thin and the water permeability is strikingly high, Jeju Island has many groundwater-preserving structures, allowing for abundant groundwater storage in the basement and large outflows through the coastal aquifer [Baek et al., 2005].

Since Jeju Island has sufficient SGD with permeable geological components, groundwater discharges in several areas along the coast. In the island, there are considerable sites where SGD is obviously detected such as Samyang Black Sand Beach, Gongcheonpo Beach, and Gwakgigwamul Beach. In order to select good study sites among multiple potential sites, several factors had been taken into account such as geological features, abundance of SGD, amount of usable data, and existence of in-situ data. In

this study, I focused on three sites: Samyang Black Sand Beach, Sinsan-ri Dock, and Oedolgae Rock. Samyang Black Sand Beach and Sinsan-ri Dock were selected for validation of the stacking method, as the SGD outflows at these sites are readily identified. In contrast, SGD has never been identified at the third study site, Oedolgae Rock, located in south Jeju Island is an isolated rock body of about 20 m height and no SGD was known to exist before. However, considering several facts including existence of springs and fish farm, I hypothesized that SGD occurs Oedolgae Rock based on three liens of evidence. The airborne TIR image displayed a feature resembling known SGD signals at this location, and this signal is unlikely to result from interferences as there are no fish farms or rivers in the area. Finally, several springs are present nearby.

In short, the first two sites were selected for validating the present stacking method and the last one was selected to locate a potential SGD site.

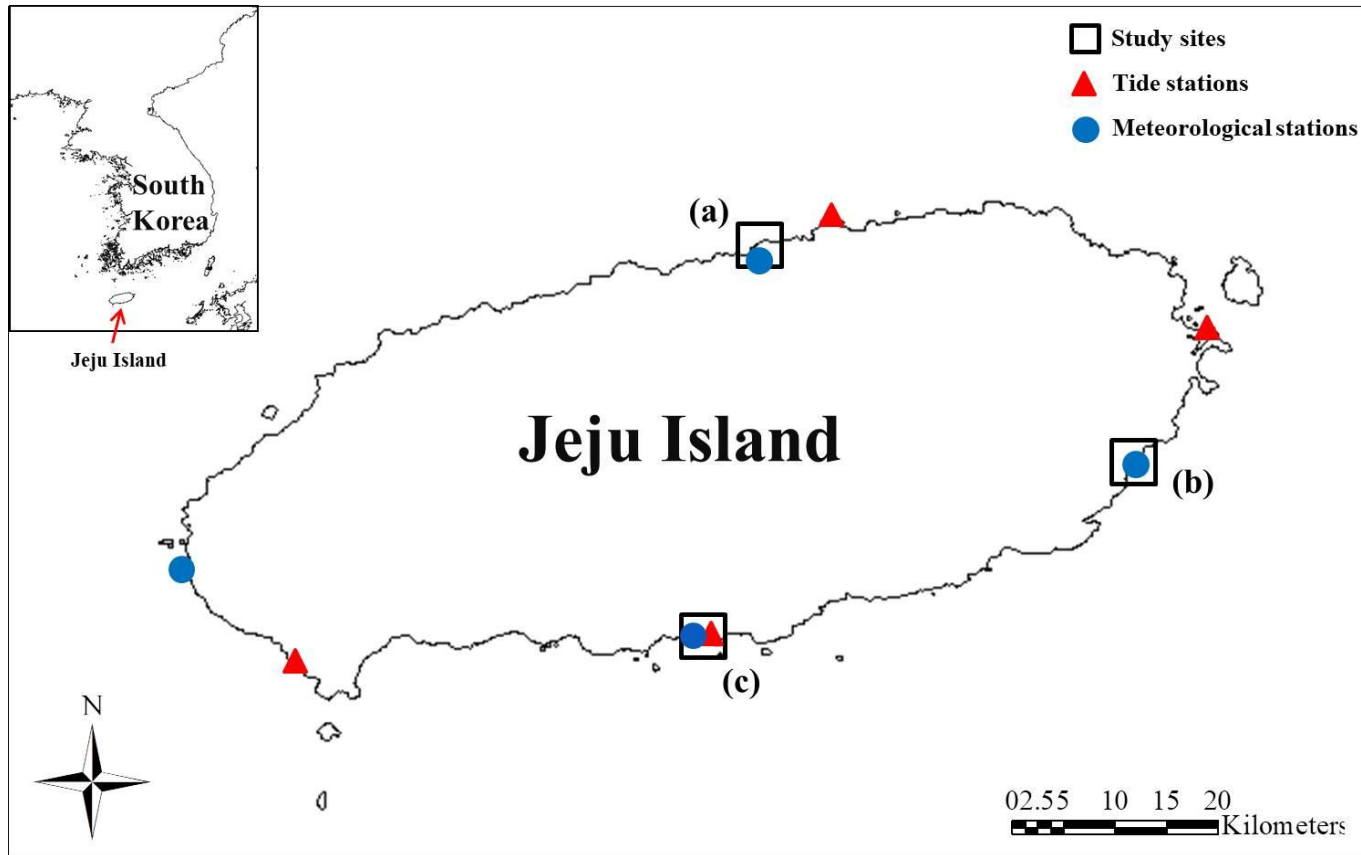


Figure 1. Map of Jeju Island showing the locations of the study sites. (a) Samyang Black Sand Beach, (b) Sinsan-ri Dock, and (c) Oedolgae Rock. The tide stations and meteorological stations on Jeju Island are showed by red triangles and blue circles, respectively.

2.2.2. Landsat Data

In this study, Landsat 5, 7 and 8 images of every month from late 2001 to 2016 were used. Because of absence of some SST data and tide data before late 2001, the Landsat data since late 2001 were used in this study. The original resolutions of the TIR band are 120 m, 60 m, and 100 m for Landsat5, 7 and 8, respectively. However, all of these were resampled and provided at a resolution of 30 m by USGS. Landsat 5 has six bands including that contains single TIR band while both Landsat 7 and Landsat 8 have two TIR bands among their bands of 8 and 11 bands, respectively. Two bands of Landsat7, band6_1 and band6_2, represent the radiance detected by the sensors of 0 to 255. Band6_1 shows the low gain with a progressive change in converting radiance and band6_2 as high gain shows a dynamic change in converting radiance [Landsat 7 Science Data Users Handbook].

Though SST fluctuates at every moment, it varies in a small temperature range. Therefore, a rapid change of SST is hard to occur in usual coastal environment. Also because I had an objective to catch the subtle differences between SST and SGD temperatures for detecting weak SGD signal which appear faintly at sea surface, I used band6_1 in this study. Landsat 7 has two TIR bands which have the same wavelength range. On the contrary, Landsat 8 has two bands, band10 and band11 which have different wavelengths to each other. In case of Landsat 8, thermal data were provided through two bands for improving accuracy of atmospheric correction. The band10 and band 11 of Landsat 8 have peaks near 11 μm and 12 μm , respectively, in the spectral response. Comparing with the two TIR bands of Landsat 7

which has a same peak at near 10.5 μm , the overlapped area between the two TIR bands of Landsat 7 and the band10 of Landsat 8 is much larger than that of between the two TIR bands of Landsat7 and the band11 of Landsat 8. Therefore, using band10 than band 11 of Landsat 8 was expected to result a similar level of error with when using Landsat 7 data in conversion process of SST. Hence, I used the band10 for the Landsat 8 data. In case of Landsat 5, it has same wavelength as the TIR bands of Landsat 7.

All Landsat data were downloaded with cloud coverage from 0 to 100 percent and filtered out if the data was cloud-covered at sub-image of the study sites. Consequently, I used 43, 40, and 43 data for stacking at Samyang Black Sand Beach, Sinsan-ri Dock, Oedolgae Rock, respectively.

Table 2. List of satellite images used in this study. The data acquisition dates and tidal conditions at the study sites.

* H: High tide, HL: High to Low tide, L: Low tide, LH: Low to High tide

Date (YYYY.MM.DD)	Satellite	*Tide (Samyang Black Snad Beach)	Tide (Sinsan-ri Dock)	Tide (Oedolgae Rock)	Spatial resolution (m)
2001.11.19	LANDSAT7	-	H	-	60
2002.01.06	LANDSAT7	L	L	L	60
2002.02.07	LANDSAT7	HL	L	L	60
2002.03.11	LANDSAT7	H	H	H	60
2002.07.17	LANDSAT7	L	-	L	60
2002.08.02	LANDSAT7	L	L	L	60
2002.09.02	LANDSAT7	L	L	L	60
2002.11.22	LANDSAT7	-	-	H	60
2003.03.30	LANDSAT7	H	HL	HL	60
2003.04.15	LANDSAT7	H	HL	HL	60
2003.05.16	LANDSAT7	H	-	-	60
2003.06.26	LANDSAT5	HL	HL	HL	120
2004.06.12	LANDSAT5	HL	L	L	120
2004.08.31	LANDSAT5	H	H	H	120
2005.02.23	LANDSAT5	H	H	H	120
2005.04.28	LANDSAT5	L	-	-	120
2006.01.25	LANDSAT5	-	H	L	120
2006.10.08	LANDSAT5	-	-	H	120
2006.10.24	LANDSAT5	H	-	-	120
2007.02.13	LANDSAT5	HL	-	-	120
2007.03.17	LANDSAT5	-	HL	HL	120
2007.05.20	LANDSAT5	H	H	H	120
2007.07.23	LANDSAT5	-	L	-	120
2007.09.25	LANDSAT5	-	-	HL	120
2008.06.07	LANDSAT5	H	-	H	120
2008.07.09	LANDSAT5	L	LH	LH	120
2008.09.27	LANDSAT5	H	-	HL	120
2008.10.13	LANDSAT5	H	HL	-	120
2008.12.16	LANDSAT5	LH	-	-	120
2009.04.07	LANDSAT5	H	HL	HL	120
2009.04.23	LANDSAT5	H	HL	HL	120
2009.05.09	LANDSAT5	-	LH	-	120
2009.06.26	LANDSAT5	-	H	H	120
2010.02.21	LANDSAT5	L	H	LH	120
2010.05.12	LANDSAT5	H	HL	HL	120
2010.09.17	LANDSAT5	-	L	L	120
2010.11.20	LANDSAT5	-	HL	HL	120
2010.12.22	LANDSAT5	-	H	H	120
2011.03.28	LANDSAT5	HL	-	-	120
2011.04.29	LANDSAT5	-	HL	HL	120
2011.09.04	LANDSAT5	L	LH	-	120
2011.10.06	LANDSAT5	-	L	H	100
2013.05.20	LANDSAT8	HL	L	L	100
2013.09.09	LANDSAT8	-	-	-	100
2013.10.27	LANDSAT8	LH	L	L	100
2014.01.31	LANDSAT8	H	H	H	100
2014.05.07	LANDSAT8	LH	L	L	100
2014.05.23	LANDSAT8	HL	-	L	100
2014.06.24	LANDSAT8	HL	-	-	100
2014.09.28	LANDSAT8	LH	-	H	100
2014.11.15	LANDSAT8	L	-	-	100
2015.02.03	LANDSAT8	H	H	-	100
2015.05.10	LANDSAT8	L	-	LH	100
2015.07.29	LANDSAT8	HL	-	-	100
2015.08.14	LANDSAT8	H	-	H	100
2016.04.10	LANDSAT8	-	H	-	100
2016.05.12	LANDSAT8	LH	L	LH	100
2016.07.31	LANDSAT8	HL	HL	HL	100
2016.10.03	LANDSAT8	-	H	H	100
2016.11.04	LANDSAT8	LH	H	LH	100

2.2.3. Airborne Data

In this study, airborne TIR images were acquired by FLIR A615 (Wilsonville, OR, USA). The spatial resolution (IFOV) of the FLIR camera is 1.23 mrad, the field of view is 45 ° x 34 °, the spectral range is 7.5 to 13 μm, the number of pixels in an image is 640 x 480 pixels, and the thermal sensitivity is less than 0.05°C at 30°C.

The airborne TIR image acquired at low tide on August 5, 2015 was used to compare with Landsat image, and to validate the application result of stacking method.

2.2.4. Comparison between Airborne Data and Landsat Data

SGD signals at all study sites in an airborne TIR image is well distinguished from the around SST. However, in two Landsat image which were acquired at similar conditions (season, SST, and tide) of airborne image, SGD signal was well detected at Samyang Black Sand Beach and Sinsan-ri Dock Landsat image while, SGD signal was not detect at Oedolgae Rock Landsat image(Table 3). In Samyang Black Sand Beach, the temperature difference between SGD temperature and SST is more than 3°C at airborne image, and about 2°C at two Landsat images. Furthermore, this temperature difference led to larger difference in SGD area.

In Sinsan-ri Dock, the temperature difference between SGD temperature and SST is about 1 and 2°C at two Landsat images, respectively. Although the temperature difference is small, the SGD area is about 1.8 and 8.4 times

larger than that of the airborne image in each case. Even in case of Oedolgae, the SGD signal was detected at airborne image, but the signal was not detected at each of two single Landsat image. This is thought to be since the temperature difference between SGD temperature and SST is quite small. Therefore, I used the stacking method to detect weak SGD signals that were certainly present but certainly not detected in a single Landsat image for low resolution.

Table. 3 Comparison between airborne data and Landsat data.

Data	Samyang Black Sand Beach		Sinsan-ri Dock		Oedolgae Rock	
	Airborne Data	Landsat Data	Airborne Data	Landsat Data	Airborne Data	Landsat Data
Date	2015.08.05	2002.08.02	2015.08.05	2002.08.02	2015.08.05	2002.07.17
		2002.09.02		2007.07.23		2002.08.02
SST (°C)	25.35	23.1	23.39	23.25	21.89	20.27
		22.85		22.55		23.4
Temperature difference between SGD temperature and SST (°C)	3.24	2.04	3.21	1.12	1.32	-
		2.28		2.07		-
SGD area (m^2)	585900	91800	295200	35100	29700	-
		107100		162000		-

2.3. Data Processing

In this study, several Landsat TIR images were used for stacking. Landsat images were acquired from USGS. From the Landsat images, I calculated radiance. Since the image data were consisted of digital numbers (DN), the process for converting DN to temperature should be firstly performed. In this process, atmospheric effects were corrected. I performed atmospheric correction using the Atmospheric Correction Parameter Calculator [Barsi, J. A., Barker, J. L., & Schott, J. R., 2003]. Using the web-based tool, I easily calculated atmospheric transmission, upwelling radiance, and downwelling radiance by converting atmospheric data to a proper format with performing the radiative transfer model. After SST was derived through the atmospheric correction, land pixels were removed by using SRTM data in 30 m spatial resolution resampled to 60 m spatial resolution. In this process, some remaining land pixels were manually removed. Then, arbitrary points with a probability of 10 percent were extracted from the offshore sea in each SST image. Using these arbitrary points, offshore SST was derived through nearest-neighborhood interpolation method. Since SGD temperature was observed at different temperatures depending on SST, just stacking of SST images may attenuate the SGD signals. Therefore, SST anomaly, subtracting offshore SST($T_{\text{offshore sea surface}}$ in eq. 5) from SST($T_{\text{sea surface}}$ in eq. 5), was required to be considered due to differences of offshore SST in each data. To stack SGD anomalies, some conditions on month and tide levels were analyzed. This step is an additional processing to detect faint SGD signals which can be missed, or confused with noise. After find optimum

month and tide level conditions, SST anomaly images satisfying the conditions were stacked. The processing step of stacking is illustrated in Figure 2.

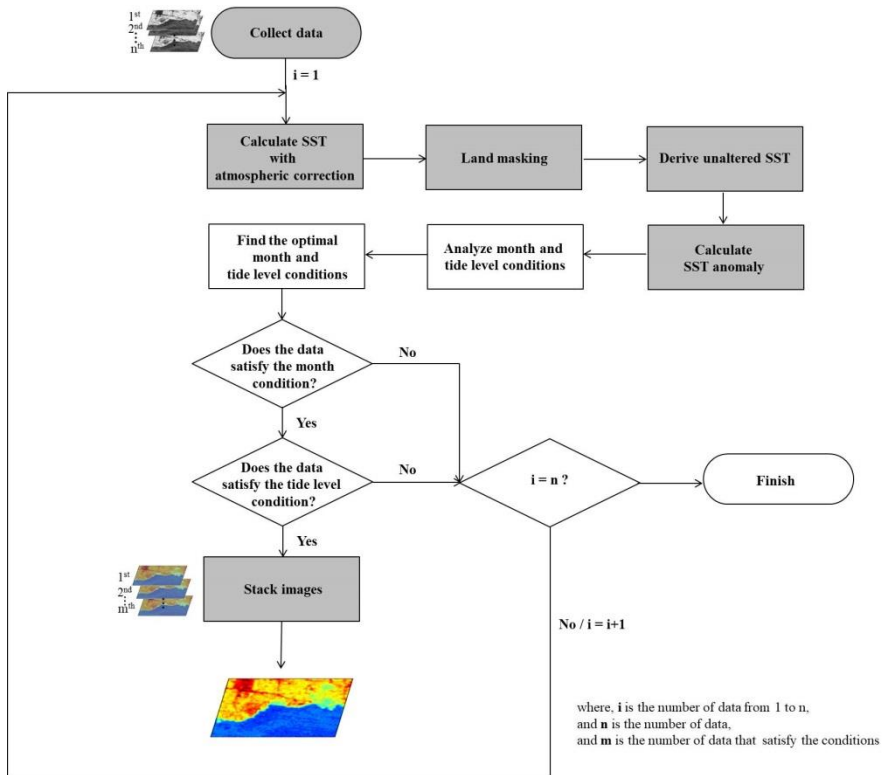


Figure 2. Flow chart for the stacking processes. The gray boxes and white boxes are essential and additional process to detect faint SGD signals, respectively.

3. Stacking Condition Analysis

3.1 Spatial and Temporal Variability of SGD

SGD always appears in different patterns by the season, wind and ocean current, even in the same area (Figure 3-5). Besides spatial and temporal variance, SGD is nearly invisible in visible light [Kelly et al., 2013]. Therefore, finding SGD outflowing location is challenging. For this reason, SGD constantly outflows, but is not always detectable from TIR images. Therefore, I analyzed the month and tidal conditions to understand when the SGD signals appeared distinctively. After determining the optimum conditions, I applied the stacking method to catch faint SGD signals.

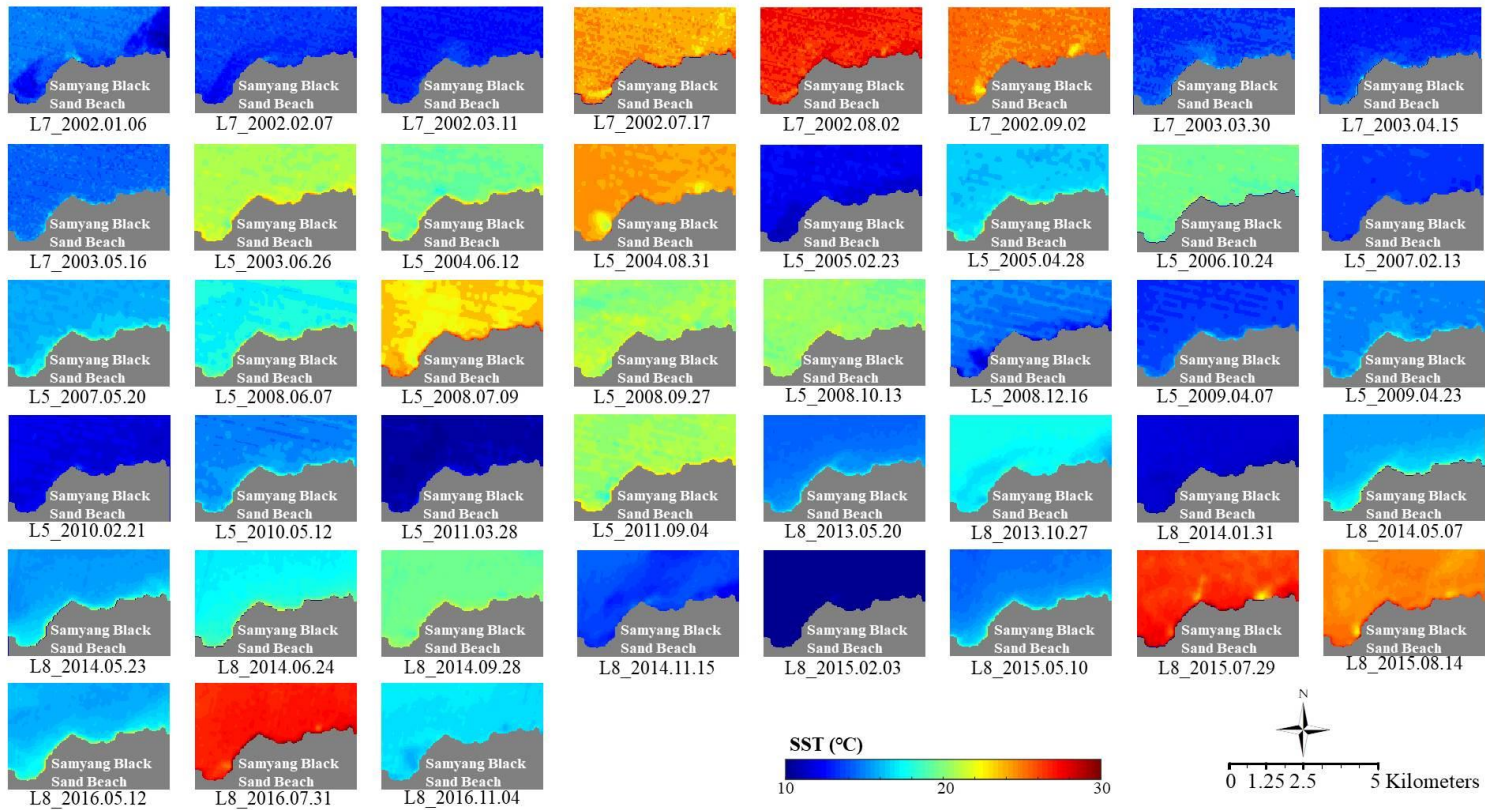


Figure 3. Landsat TIR images at each date in Samyang Black Sand Beach. L5, L7 and L8 refer to Landsat_5, Landsat_7 and Landsat_8, respectively. The spatial resolutions of the TIR band of the Landsat satellites are 120 m, 60 m, and 100 m for L5, L7, and L8, respectively.

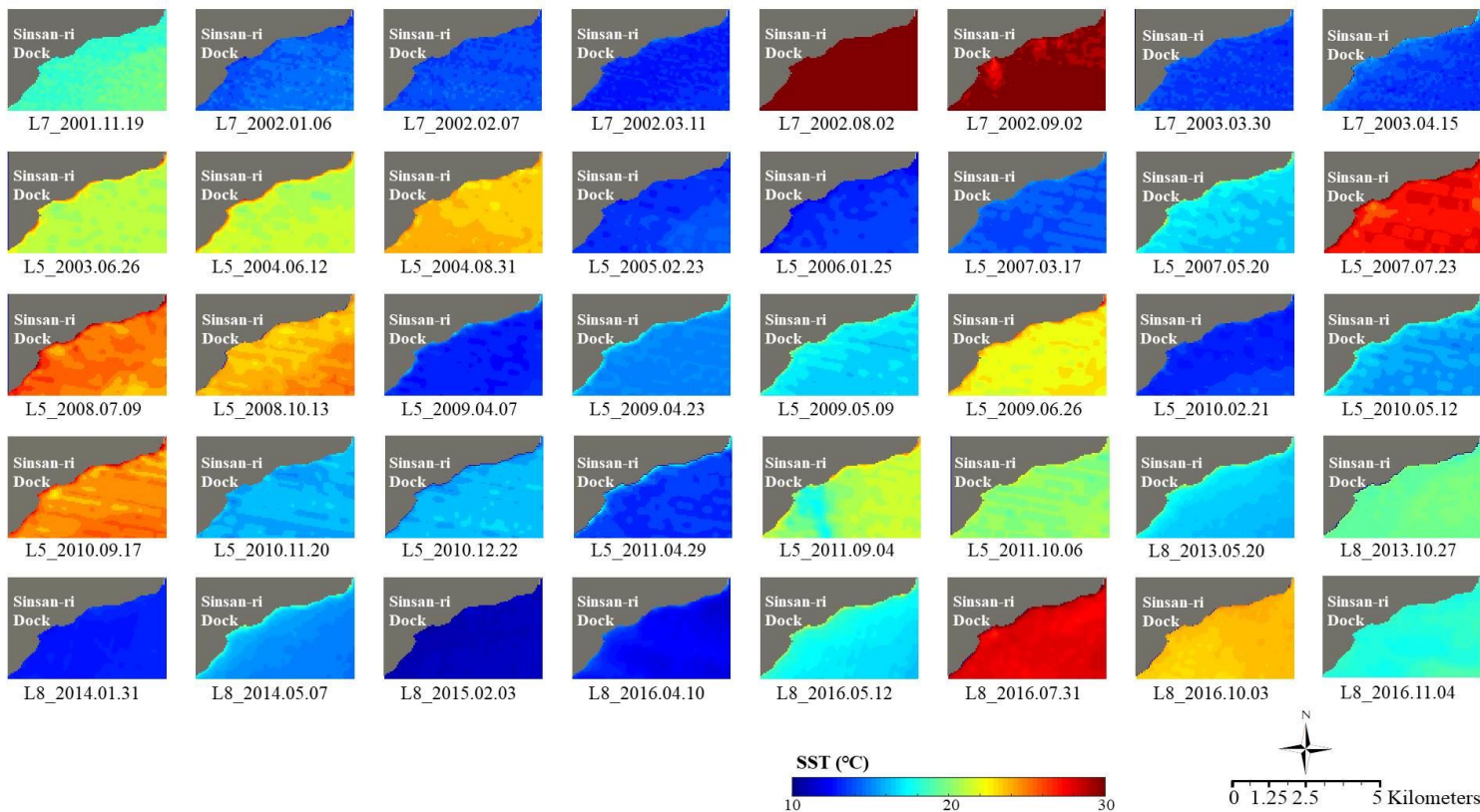


Figure 4. Landsat TIR images at each date in Sinsan-ri Dock. L5, L7 and L8 refer to Landsat_5, Landsat_7 and Landsat_8, respectively. The spatial resolutions of the TIR band of the Landsat satellites are 120 m, 60 m, and 100 m for L5, L7, and L8, respectively.

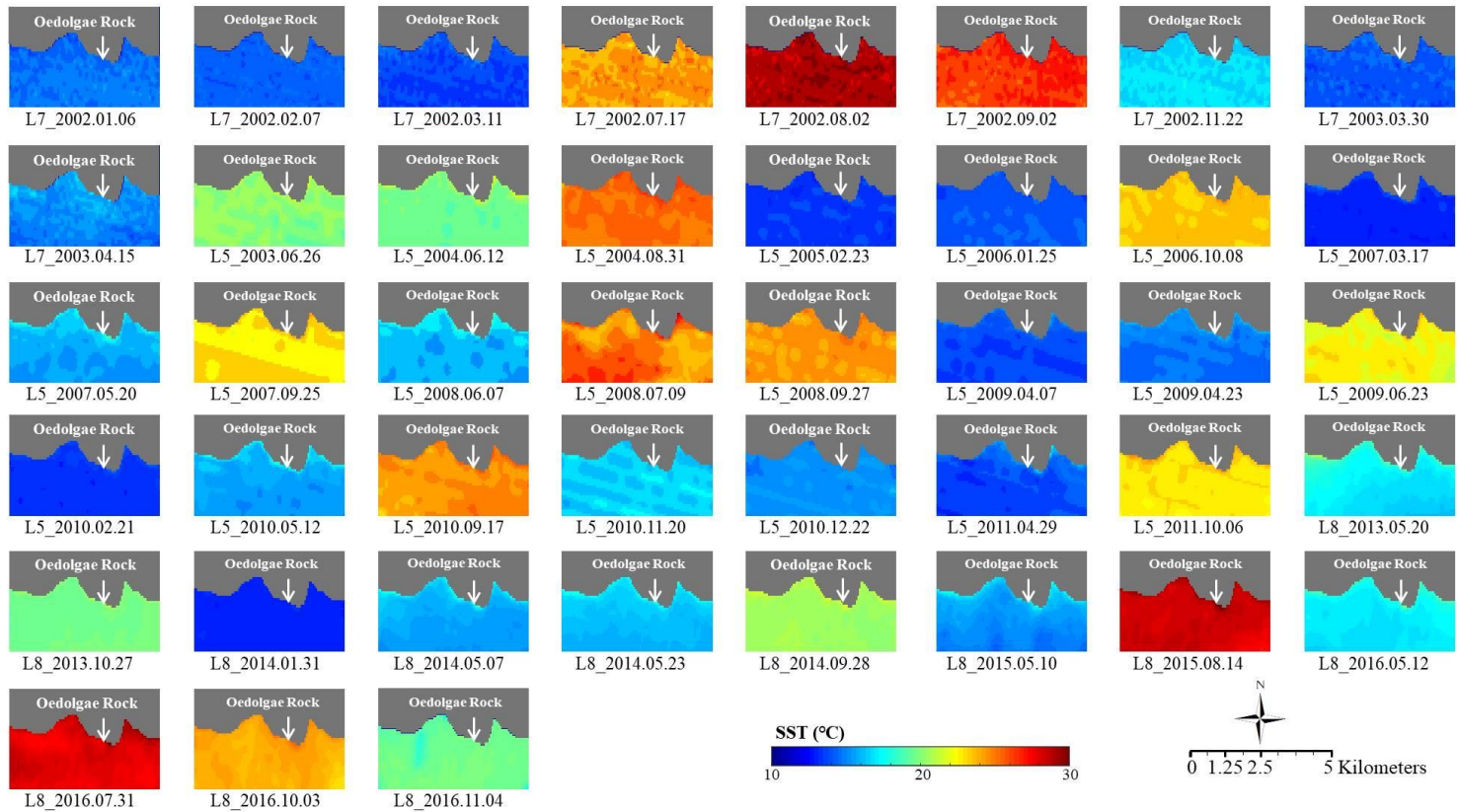


Figure 5. Landsat TIR images at each date in Oedolgae Rock. L5, L7 and L8 refer to Landsat_5, Landsat_7 and Landsat_8, respectively. The spatial resolutions of the TIR band of the Landsat satellites are 120 m, 60 m, and 100 m for L5, L7, and L8, respectively.

3.2 Relation between SST and SST Anomalies

Although SGD is constantly outflowing, its signal may not be captured by TIR remote sensing because of several factors such as variations in SST, tide, and geological features. SST is one of most crucial factors in the SGD signal detection in the TIR remote sensing. SGD temperatures generally range from 15 to 17°C throughout the year on Jeju Island [Park et al., 2014]. Considering the average SST near Jeju Island are 16.5, 27, 18 and 15°C in spring, summer, autumn, and winter, respectively, some problems occur to detect SGD in multiple TIR images except in the summer season [Park et al., 2014]. Furthermore, SST anomaly had negative values when SST was about 20°C or higher in all study sites (Figure 6). Hence, after examining the SST anomaly as a function of SST, I analyzed the relationship between month of year and the SST anomalies.

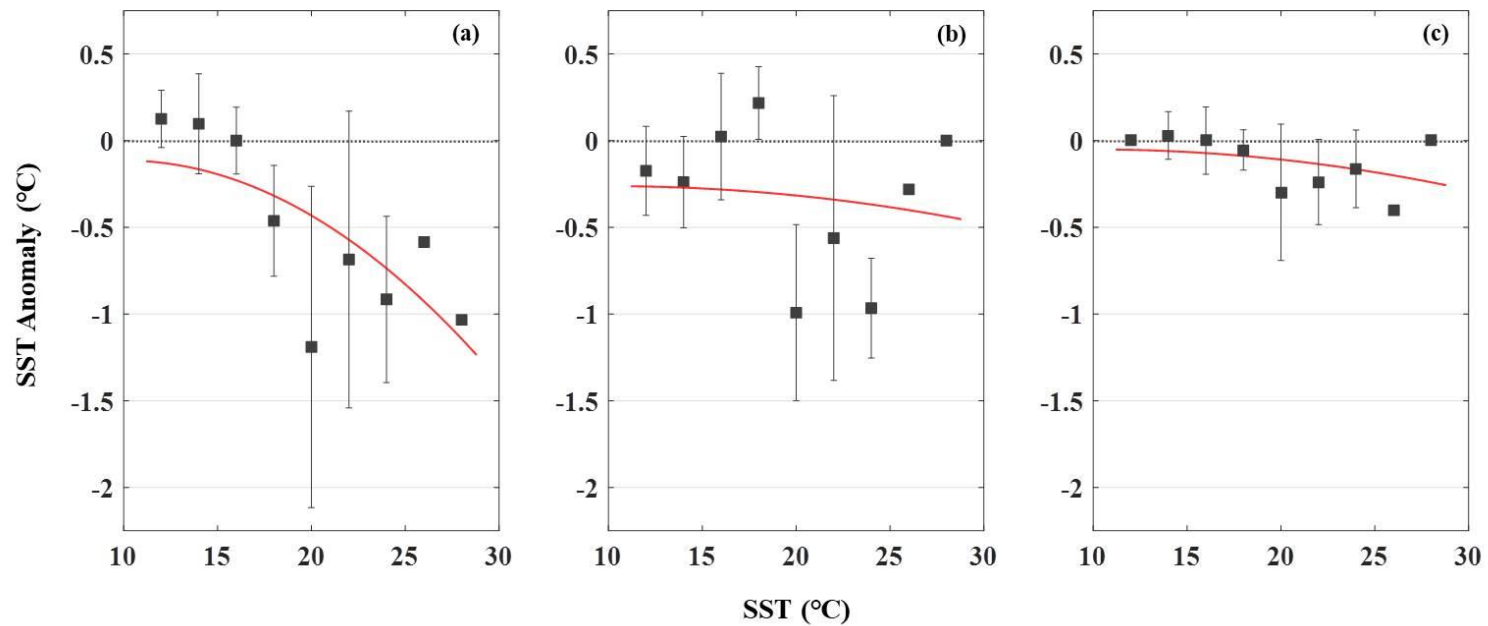


Figure 6. SST anomalies as a function of SST at each site. (a) Samyang Black Sand Beach, (b) Sinsan-ri Dock, and (c) Oedolgae Rock.

3.3 Monthly Analysis of SST Anomaly

Monthly analysis of SST anomaly indicates a clear periodic pattern at all sites (Figure 7a-c). The SST anomalies have their little positive values in the spring (March to May) and large negative values in the summer (June to September). Such a seasonal variation is more distinctive at Samyang Black Sand Beach and Sinsan-ri Dock (Figure 7a & b) than Oedolgae Rock (Figure 7c). This may be due to the differences in strength and amount of SGD for each study sites. At Samyang Black Sand Beach and Sinsan-ri Dock (Figure 7a & b), most SST anomalies were in the range of -2 to 1°C. Whereas, the SST anomaly at Oedolgae Rock site was in range of -1 to 0.5°C. This range is relatively narrower than that of the two preceding sites. This is may be due to water depth of Oedolgae site is higher than that of other two sites. Also, as mentioned before, since both strength and quantity of SGD varied site by site, SST anomalies have different ranges, too.

Detecting SGD signal is easier in midsummer (normally, July to August) than other seasons since SST is higher than 20°C in the midsummer while SGD is generally known to average about 16°C throughout the year. Considering the relatively constant SGD temperature, therefore, it is difficult to detect SGD signals in TIR images except the summer [Park et al., 2014]. Though SGD is mixed with seawater, the SGD temperature at sea surface is still lower than offshore SST in the summer. Thus, SGD signal is easily detected in summer season but in winter due to such a temperature characteristic. Nevertheless, some cold plumes regarded as SGD signals appeared in some winter images at Samyang Black Sand Beach and Sinsan-

ri Dock (Figure 7a & b). Especially, the cold plumes were more clearly appeared in two images in Samyang Black Sand Beach. The SGD temperatures in the two images were in the range of 11 to 13°C which were slightly lower than the average SGD temperature. These two images were acquired on January 6, 2002 at low tide and December 16, 2008 at high to low tide (midrising). Among several possibilities I believe thought that strong outflowing of SGD, shallow depth of springs, and high SST are the main reasons for the appearance of cold plumes in winter season.

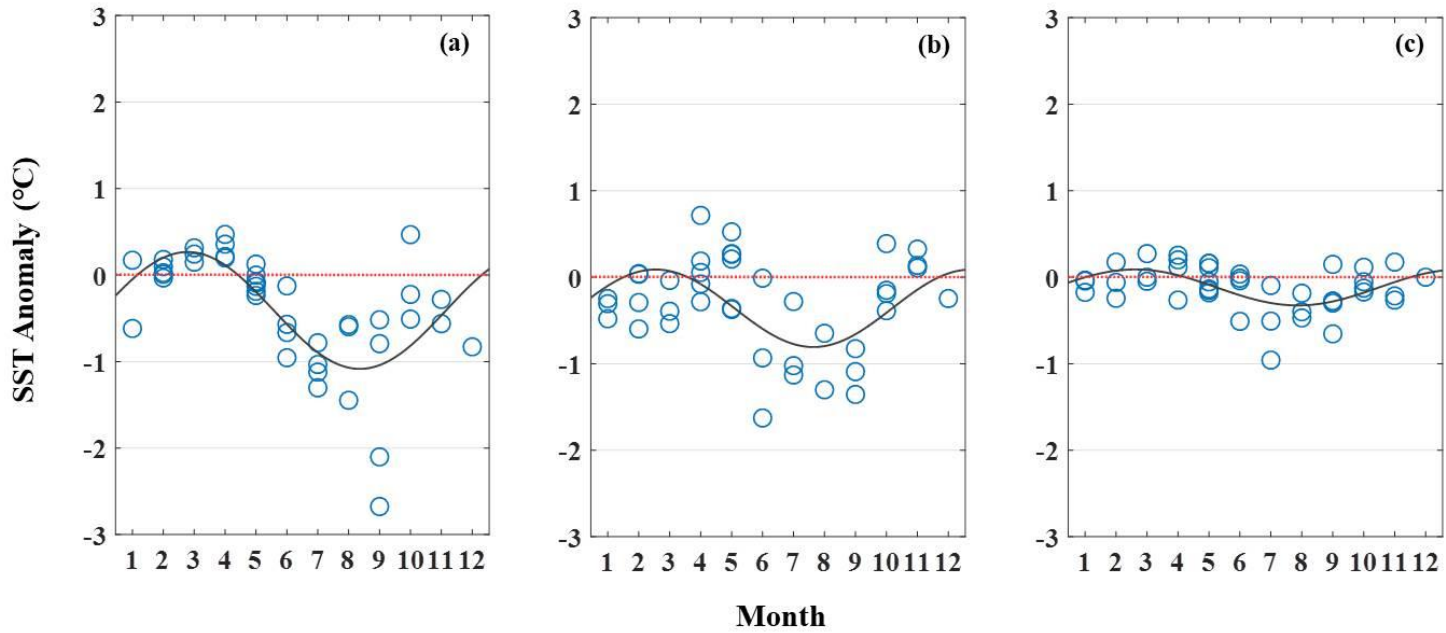


Figure 7. SST anomalies according to month of year at each site. (a) Samyang Black Sand Beach, (b) Sinsan-ri Dock, and (c) Oedolgae Rock.

3.4 Tidal Analysis of SST Anomaly

As shown in Figure 7, most SST anomalies appeared in strong negative values from June to September. After September, the SST anomalies were gradually changed from negative to positive values. The peaks are in March and the positive SST anomalies last until June. However, since these peaks are quite smaller than peaks in negative, positive values are not considered as meaningful SGD signals.

To find the optimum conditions of SGD detection and reduce possibility of missing weak SGD signals, I examined SST anomaly as a function of tide level between June and September. Considering the seasonal average SST and the SGD temperature, and as mentioned before, since negative SST anomaly was thought to be SGD signal and I did not consider positive SST anomalies. Therefore, I analyzed only negative SST anomalies in the summer data which are located below the red line in Figure 7.

In this study, four tide stages were defined: high tide (H), midebbing (HL), low tide (L), midrising (LH). High tide and low tide are defined as the highest and lowest points of the tidal cycle, respectively, and data within a ± 30 cm range of those points were judged as H or L. The data out of that range were defined as HL or LH depending on the tide level is decreasing or increasing, respectively. Since I classified the tide level based on relative values, quantitative comparisons among different tide levels were not conducted.

In all study sites, SST anomaly was the strongest during low tide and the weakest during high tide (Figure 8). In this analysis, SST anomaly in

Oedolgae Rock appeared in a relatively narrower range than those of other two sites like SST anomaly and month analysis (Figure 8c).

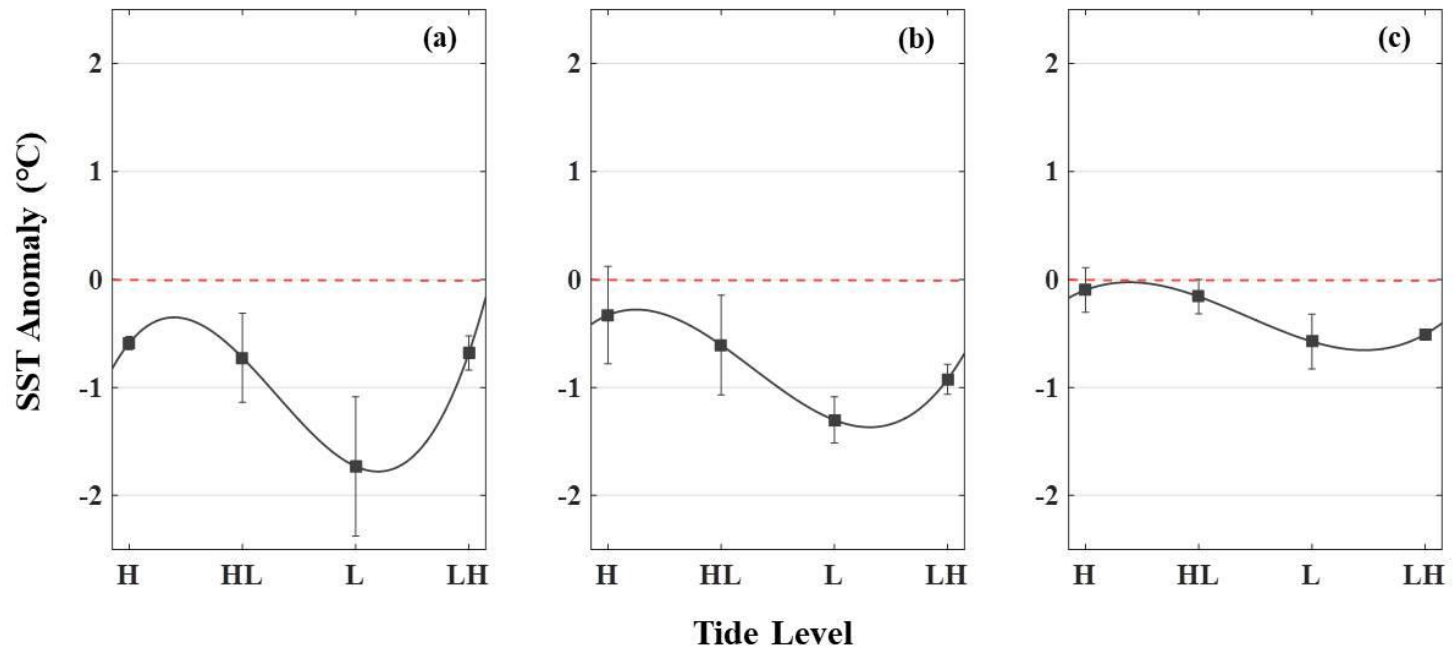


Figure 8. SST anomalies according to tide level (H: High, HL: High to Low(midebbing), L: Low, LH: Low to High(midrising)) between June and September at each site. (a) Samyang Black Sand Beach, (b) Sinsan-ri Dock, and (c) Oedolgae Rock.

3.5 Stacking Condition Analysis with NEdT

The NEdT of the Landsat TIR bands are 0.17-0.30 K at 280 K for Landsat5, 0.28 K at 280 K for low gain band(6_1 band) of Landsat7, 0.4 K at 300 K, and 0.27 K at 360 K for band10 of Landsat8 [Irons et al., 2012]. The SST of the three study sites had an average of 17 to 19°C and entirely distributed in the range between 10 and 30°C. Since it is the closest to the average SST, NEdT for band10 of Landsat 8 at 300 K (red line in Figure 9) was used to analyze the influence of NEdT on image stacking.

In Figure 9, the SGD signals were hard to discern from the offshore SST when the SST anomalies were above the red dotted line at -0.4°C while easily identifiable below it.

As previously mentioned, stacking SST anomalies without considering difference of SST may diminish SGD signals. The average SST anomalies all data were -0.37°C, -0.30°C, and -0.12°C for Samyang Black Sand Beach, Sinsan-ri Dock, and Oedolgae Rock, respectively ('All' in Table 4). SST anomalies obtained by averaging all data are smaller than NEdT at all sites. This means that SGD signals are undetectable under this condition, and, accordingly valuable SGD signals can be missed. Hence, SST anomalies should be only under the optimum month and tide level conditions. Of course, Samyang Black Sand Beach and Sinsan-ri Dock have greater SST anomalies than NEdT when SST anomalies are negative (red and blue squares in Figure 9). In these sites, most SGD signals are discernable in an individual image. For Oedolgae Rock sites, however, SGD signals are hard to detect from a single image (black squares in Figure 9). Even the average

SST anomaly is lower than NEdT in the summer season ('Summer' in Figure 9). From this, I found that simply considering seasonality is not enough to detect faint signals. Therefore, I analyzed tidal condition to catch a subtle difference between SGD temperatures and SSTs. SST anomalies were 2.62, 2.32, 2.38 times larger at low tide in summer ('Summer Low tide' in Table 4) than SST anomalies ('Negative Values' in Table 4) in Samyang Black Sand Beach, Sinsan-ri Dock, and Oedolgae Rock, respectively. Considering both month and tidal conditions, SST anomalies were successfully detected in Oedolgae Rock. In Oedolgae Rock, the average SST anomalies under all conditions but at low tide in the summer ('Summer Low tide' in Table 4) were not in the confidence temperature range (CTR) to discern SGD signal from SST. The CTR means the range between the black and the red dotted line in Figure 9. Therefore, SGD signals are hard to detect in a single TIR image even in a summer season at this site. However, the signals at Oedolgae Rock were detectable even in data at low tide in the summer (black point at 'Summer Low tide' in Figure 9). Hence, stacking TIR images acquired at low tide in the summer is a very effective and powerful way to detect faint SGD signals.

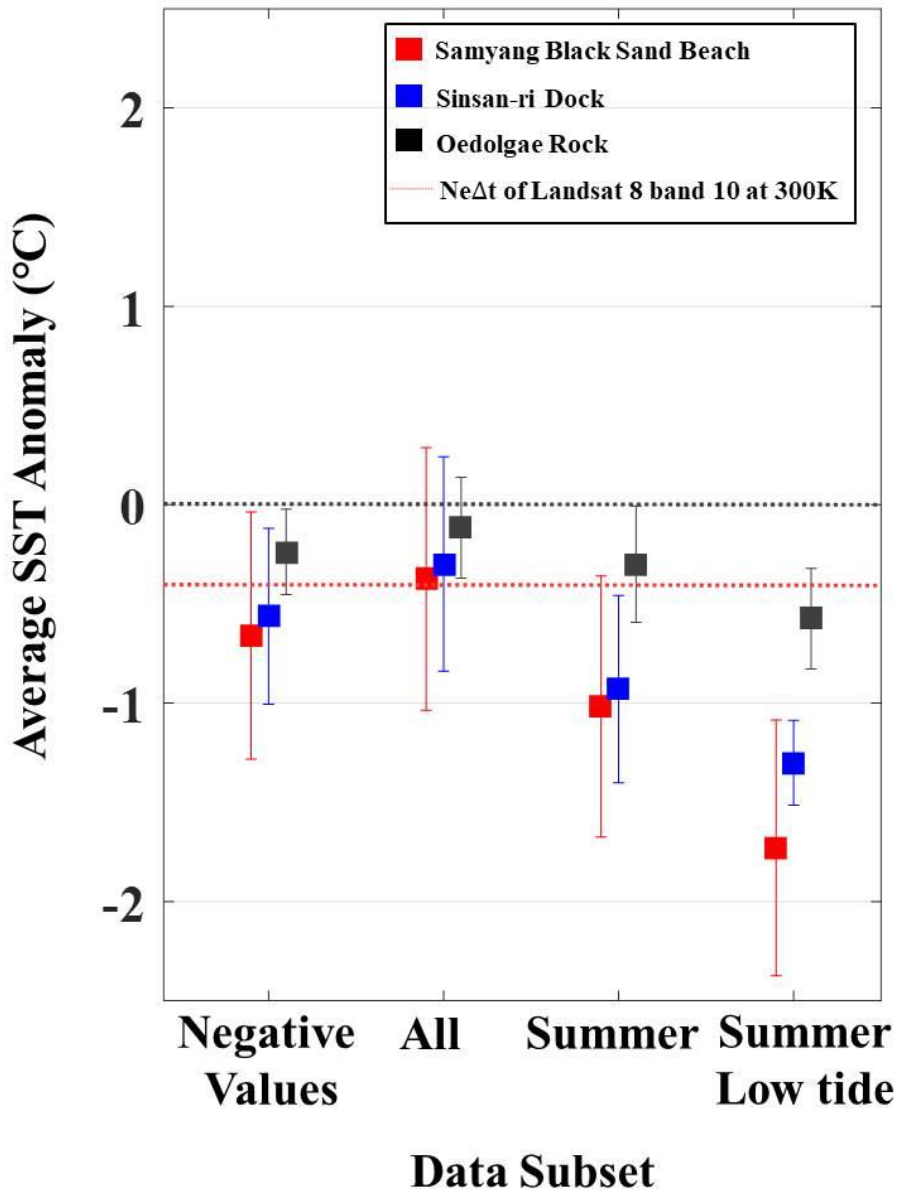


Figure 9. Average SST anomaly for three different stacking conditions as well as all the data. The conditions used to define the stacking conditions are described in Table 3. The red line shows the NEΔt of the Landsat data.

Table 4. The averages SST anomalies for the four stacking conditions. Number of data refers to the number of images fulfilling each condition.

		*A: Samyang Black Sand Beach	B: Sinsan-ri Dock	C: Oedolgae Rock	
SST Anomaly Stacking Condition	Description	*Number of Data	Samyang Black Sand Beach	Sinsan-ri Dock	Oedolgae Rock
All	Data from January to December between 2002 and 2016	A : 43 B : 40 C : 43	-0.37	-0.30	-0.12
Summer	Data from June to September between 2002 and 2016	A : 15 B : 11 C : 15	-1.02	-0.93	-0.30
Summer Low Tide	Low tide data of Summer	A : 5 B : 5 C : 5	-1.73	-1.30	-0.57
Negative Values	Data likely to be an SGD signal showing negative anomaly in all data	A : 29 B : 27 C : 29	-0.66	-0.56	-0.24

4. Stacking Landsat Data Satisfying the Optimum Condition

4.1 Stacking Under the Optimum Condition

Even in the sites where SGD occurs in abundant, its signals may not be detectable depending when the images were acquired. Furthermore, in such areas detecting its signals is difficult even if using an image at low tide in the summer. Also SGD may appear differently depending on their occurrence time even at same tidal condition. Hence, judging existence of SGD using only a single image is not adequate.

Based on the previous results of month and tidal condition analysis, I applied the stacking method to the three study sites according to optimum conditions. Summer data and low tide in summer data were stacked. For summer data stacking, 15, 11, and 15 images were stacked at Samyang Black Sand Beach, Sinsan-ri Dock, Oedolgae Rock, respectively. Five SST anomaly images which were acquired at low tide in summer were stacked at each study sites (Figure 10b, 11b & 12b).

The result of stacking summer data, SGD signals appeared strongly in both Samyang Black Sand Beach and Sinsan-ri Dock (Figure 10a & 11a), while, it was hard to discern in stacked image of Oedolgae Rock (Figure 12a). However, when applying a low tide condition, the SGD signal appeared at Oedolgae Rock (Figure 12b), and more distinctively appear than that of summer condition at Samyang Black Sand Beach and Sinsan-ri Dock

(Figure 10b & 11b).

In Samyang Black Sand Beach (Figure 10b), three distinct signals were discernable from the sea surface. The strong signal near $126^{\circ}35'$ E has previously known as a SGD springs [Bong Joo Lee et al., 2002]. The signal near $126^{\circ}34'40''$ E was the one from a river since it is closer to the cold plume than the SGD spring nearby. Another distinctive signal, between $126^{\circ}35'$ E and $126^{\circ}36'$ E, was caused probably by cooling water from a thermoelectric power plant.

In Sinsan-ri Dock (Figure 11b), one strong signal near $126^{\circ}53'$ E and a weak one near $126^{\circ}54'$ E were identified. Since there are SGD springs and fish farms near this site, the strong signal was apparently affected by them. However, the weak signal near $126^{\circ}54'$ E seemed to be due to seral fish farms nearby. The SGD signal in Oedolgae Rock (Figure 12b) was not as strong as those in Samyang Black Sand Beach and Sinsan-ri Dock (Figure 10b & 11b). Unlike SGD signal of both Samyang Black Sand Beach and Sinsan-ri Dock sites, the SGD signal of Oedolgae Rock site was not as strong as that of other sites. Although the signal was not strong as other sites in the stacked SST anomaly image, it was regarded as a meaningful signal. Since there were no confusing factors such as fish farms and, the signal near $126^{\circ}33'$ E was probably caused by SGD.

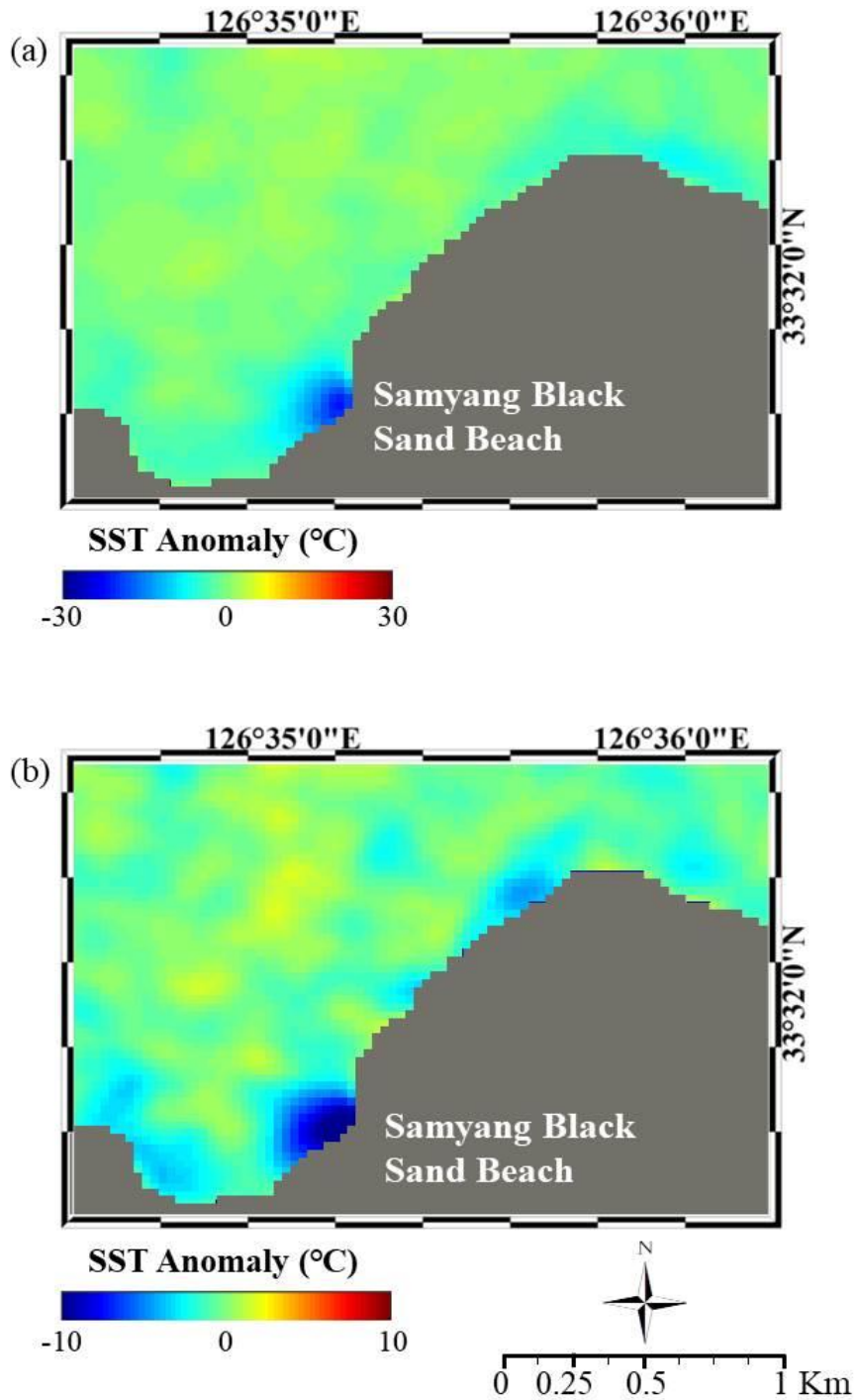


Figure 10. Images of stacked SST anomalies corresponding to each conditions at Samyang Black Sand Beach. (a) Summer condition (b) Low tide in summer condition.

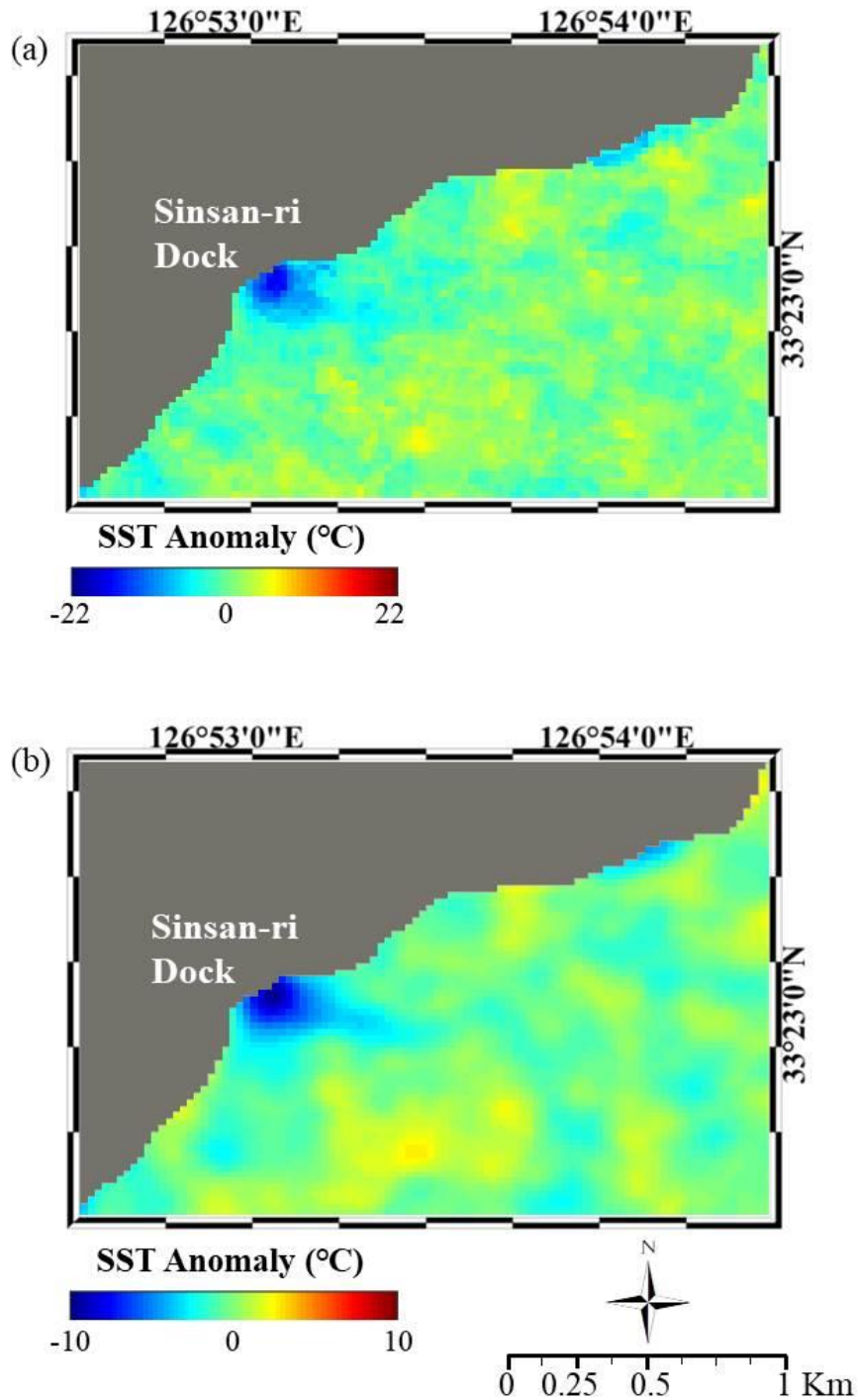


Figure 11. Images of stacked SST anomalies corresponding to each conditions at Sinsan-ri Dock. (a) Summer condition (b) Low tide in summer condition.

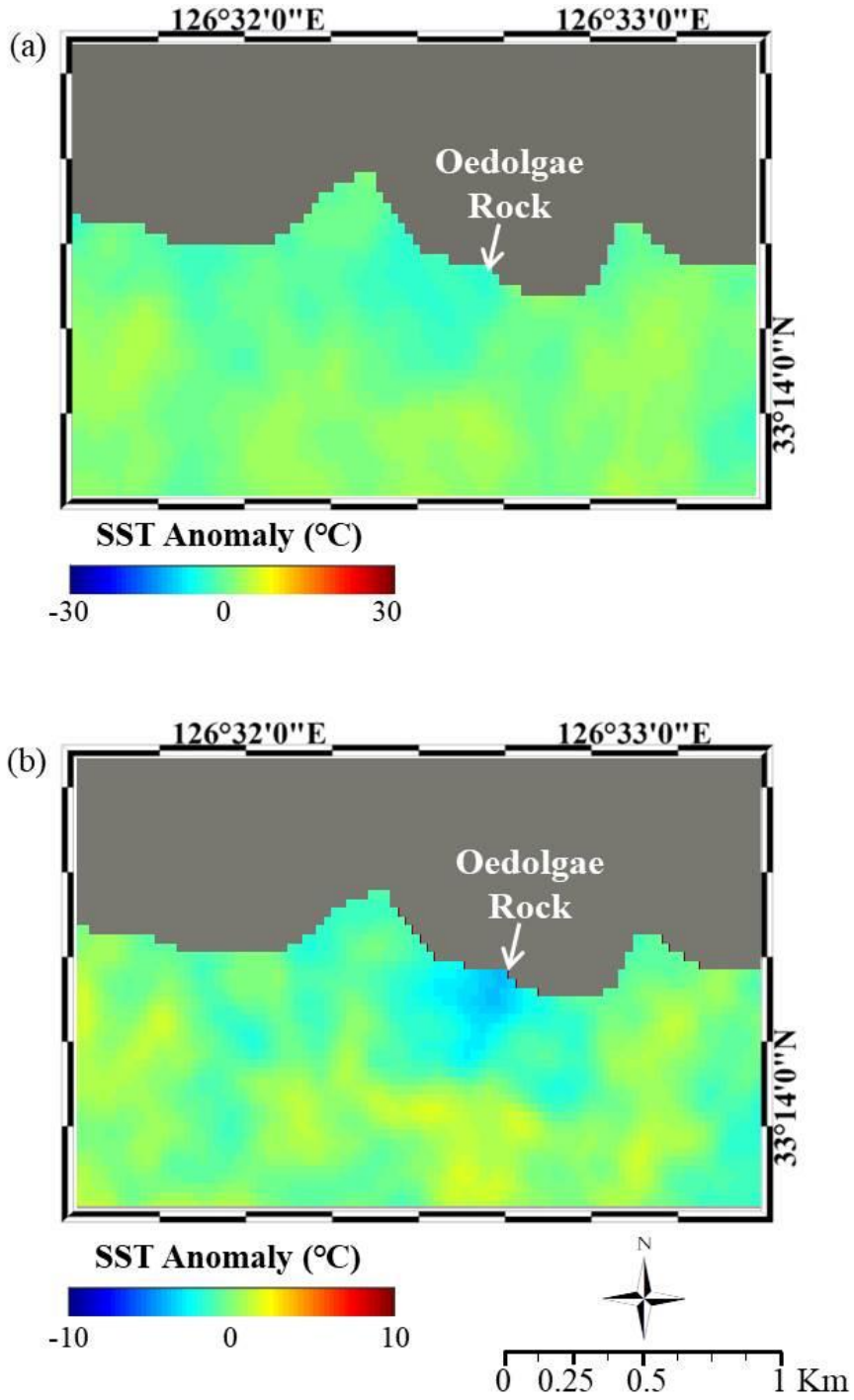


Figure 12. Images of stacked SST anomalies corresponding to each conditions at Oedolgae Rock. (a) Summer condition (b) Low tide in summer condition.

4.2 Validation with Airborne Data

To validate that the SGD signal in the stacked image is reliable, I used mosaicked airborne data. Their super precision up to 0.05°C at 30°C and high spatial resolution of 0.6 m enable to verify faint SGD signals that were newly founded in the stacked image of SST anomalies. The airborne image was also used to check other SGD signals detected in Landsat images and to compare the difference between SST and SGD temperature.

In Samyang Black Sand Beach and Sinsan-ri Dock, several cold plumes clearly appeared in the airborne image (Figure 13a & b). While, in Oedolgae Rock, the SGD anomaly which is weaker than in the other two sites appeared in airborne image (near 126 °33' E in Figure 13c). Comparing through figure 10 to 12 with figure 13c, the SGD locations are matched well in both stacked and airborne images in all study sites.

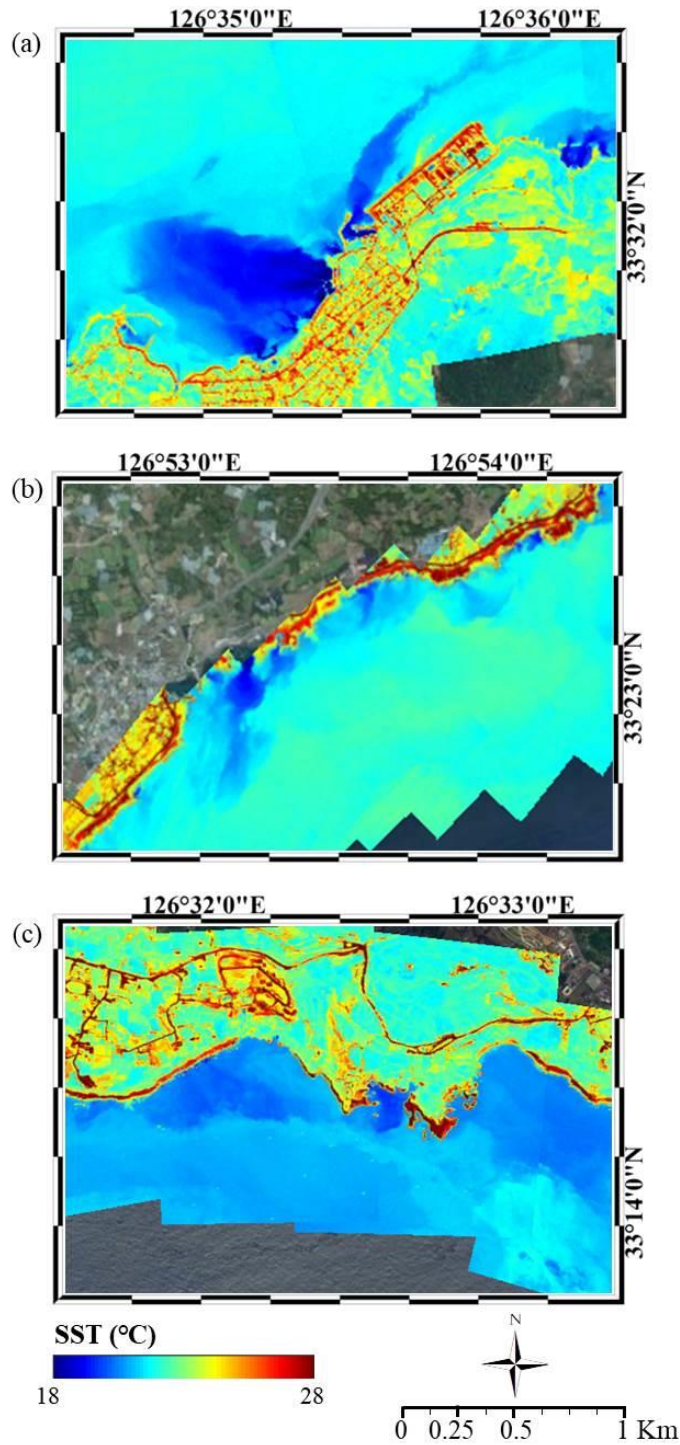


Figure 13. Airborne TIR images acquired at low tide on August 5, 2015 at each study sites. (a) Samyang Black Sand Beach, (b) Sinsan-ri Dock, and (c) Oedolgae Rock.

5. Conclusion

I showed that the stacking method is an effective tool (1) to confirm the existence of SGD which varies both in time and space, and sometimes disappears due to several factors such as low mean SST and tidal conditions, and (2) to detect weak SGD signals that are usually undetectable in a single Landsat TIR image. Firstly, I applied this method at two sites nearshore Jeju Island where SGD signals appeared clearly. Then, the method was applied to another site having a potential SGD. Although SGD appeared in various patterns and of different amplitudes with time, the stacking method was turned out to be very powerful way to detect SGD with space-borne remote sensing data of low resolution in a local scale. Even where SGD signals were hardly visible, the method enabled to indicate its existence.

At Oedolgae Rock, detection of SGD in a single space-borne image was more difficult than other sites due to weaker signals. The average SST anomaly was -0.24°C and it was lower than NEdT of Landsat. The average SST anomaly in this site was -0.30°C even in summer, which was slightly lower than NEdT of Landsat. However, the average SST anomaly of low tide in summer was -0.57°C , which was a little higher than NEdT. When stacking all the SST anomalies, the noise also increased with SGD signals. Hence, reliable SGD signal detection is possible when stacking images of low tide in summer where the SGD signals are reliably detected.

While SGD mostly appears in summer, some distinctive SGD signals also appeared in winter at Samyang Black Sand Beach and Sinsan-ri Dock. The

SGD signals at Sinsan-ri Dock were not clearly discernable from the SST. However, some SGD signals apparently appeared at two images of Samyang Black Sand Beach, acquired at low tide on January 6, 2002 and midrising on December 16, 2008. The average SSTs of the three sites at each date were similar, with values of 14 and 17°C, respectively. However, some distinct SGD was detectable in Landsat data acquired in winter due to its larger amount and greater strength at Samyang Black Sand Beach than the other two sites. Unlike the fact that only summer data is known to be able to detect SGD signals in Jeju Island, the temperature of SGD was showed lower than SST at two of winter data. Also, a few positive SST anomalies were observed, but it did not show a clear temperature differences to be considered as a SGD signal.

This study demonstrated that quite faint SGD signals could be detected by Landsat image if using the stacking method. It is also worth noting that this approach can be applied into the general cases. In this study, the average SGD temperature and average SST are the values of Jeju Island which is located near 36° north. If the mean values of SST and SGD temperature are available, the approach proposed in this study can be easily applied into the general cases.

Reference

Al Bassam, A. A., & Tiro, H. M. (2013). Using Remote Sensing and GIS for Submarine Freshwater Springs Exploration as a Plausible Water Source in Saudi Arabia. *International Journal of Geosciences and Geomatics*, Vol.1, Issue 1

Barsi, J. A., Barker, J. L., & Schott, J. R. (2003). An atmospheric correction parameter calculator for a single thermal band earth-sensing instrument. In *Geoscience and Remote Sensing Symposium, 2003. IGARSS'03. Proceedings. 2003 IEEE International* (Vol. 5, pp. 3014-3016). IEEE.

Barsi, J. A., Schott, J. R., Palluconi, F. D., Helder, D. L., Hook, S. J., Markham, B. L., ... & O'Donnell, E. M. (2003). Landsat TM and ETM+ thermal band calibration. *Canadian Journal of Remote Sensing*, 29(2), 141-153.

Baek, S. G., & Park, M. E. (2005). Exploration and Verification of Submarine Groundwater Discharge on Jeju Island by Remotely Sensed Based water Quality Analysis. *Economic and Environmental Geology*, 38(4), 395-409.

Beck, A. J., Rapaglia, J. P., Cochran, J. K., & Bokuniewicz, H. J. (2007). Radium mass-balance in Jamaica Bay, NY: evidence for a substantial flux of

submarine groundwater. *Marine Chemistry*, 106(3), 419-441.

Becker, M. W. (2006). Potential for satellite remote sensing of ground water. *Ground water*, 44(2), 306-318.

Bong Joo Lee, Sang Ho Moon, Ki Hwa Park, Dongchan Koh and Ki Won Koh. (2002). Hydrogeochemical characteristics of of the spring waters in Jeju. *Journal of the geological society of Korea*, 38(3), 421-439.

Burnett, W. C., Taniguchi, M., & Oberdorfer, J. (2001). Measurement and significance of the direct discharge of groundwater into the coastal zone. *Journal of Sea Research*, 46(2), 109-116.

Chander, G., Markham, B. L., & Helder, D. L. (2009). Summary of current radiometric calibration coefficients for Landsat MSS, TM, ETM+, and EO-1 ALI sensors. *Remote sensing of environment*, 113(5), 893-903.

Cyronak, T., Santos, I. R., Eler, D. V., Maher, D. T., & Eyre, B. D. (2014). Drivers of pCO₂ variability in two contrasting coral reef lagoons: The influence of submarine groundwater discharge. *Global Biogeochemical Cycles*, 28(4), 398-414

French, A. N., Norman, J. M., & Anderson, M. C. (2003). A simple and fast atmospheric correction for spaceborne remote sensing of surface

temperature. *Remote Sensing of Environment*, 87(2), 326-333.

Gobler, C. J., & Sañudo-Wilhelmy, S. A. (2001). Temporal variability of groundwater seepage and brown tide blooms in a Long Island embayment. *Marine Ecology Progress Series*, 217, 299-309.

Irons, J. R., Dwyer, J. L., & Barsi, J. A. (2012). The next Landsat satellite: The Landsat data continuity mission. *Remote Sensing of Environment*, 122, 11-21.

Kang, D. H., Yang, S. I., Kim, T. Y., Park, H. J., & Kwon, B. H. (2008). The variation characteristics of groundwater level with distance from shoreline in the Jeju Island. *The Journal of Engineering Geology*, 18(2), 167-176.

Kelly, J. L., Glenn, C. R., & Lucey, P. G. (2013). High-resolution aerial infrared mapping of groundwater discharge to the coastal ocean. *Limnol. Oceanogr.: Methods*, 11, 262-277.

Knee, K., & Paytan, A. (2011). 4.08 submarine groundwater discharge: a source of nutrients, metals, and pollutants to the Coastal Ocean. *Treatise Estuar. Coast. Sci*, 4, 205-234.

LaRoche, J., Nuzzi, R., Waters, R., Wyman, K., FALKOWSKI, P., & WALLACE, D. (1997). Brown tide blooms in Long Island's coastal waters

linked to interannual variability in groundwater flow. *Global Change Biology*, 3(5), 397-410.

Lee, E., Kang, K. M., Hyun, S. P., Lee, K. Y., Yoon, H., Kim, S. H., ... & Ha, K. (2016). Submarine groundwater discharge revealed by aerial thermal infrared imagery: a case study on Jeju Island, Korea. *Hydrological Processes*, 30(19), 3494-3506.

Mallast, U., Siebert, C., Wagner, B., Sauter, M., Gloaguen, R., Geyer, S., & Merz, R. (2013). Localisation and temporal variability of groundwater discharge into the Dead Sea using thermal satellite data. *Environmental earth sciences*, 69(2), 587-603.

Masqué, P. (2012). Methodological study of submarine groundwater discharge from a karstic aquifer in the Western Mediterranean Sea. *Journal of Hydrology*, 464, 27-40.

Moore, W. S. (1999). The subterranean estuary: a reaction zone of ground water and sea water. *Marine Chemistry*, 65(1), 111-125.

Moore, W. S. (2010). The effect of submarine groundwater discharge on the ocean. *Annual Review of Marine Science*, 2, 59-88

NASA, (2009). Landsat 7 Science Data Users Handbook, Chapter 2. 11:117-

120. Available from: < https://landsat.gsfc.nasa.gov/wp-content/uploads/2016/08/Landsat7_Handbook.pdf>.

Paerl, H. W. (1997). Coastal eutrophication and harmful algal blooms: Importance of atmospheric deposition and groundwater as “new” nitrogen and other nutrient sources. *Limnology and oceanography*, 42(5part2), 1154-1165

Park, J. M., Kim, D. H., Yang, S. K., & Yoon, H. J. (2014). A Study on Estimation of Submarine Groundwater Discharge Distribution Area using Landsat-7 ETM+ images around Jeju island. *The Journal of the Korea institute of electronic communication sciences*, 9(7), 811-818.

Park, J. M., & Yoon, H. J. (2013). A Study on Estimation of Submarine Groundwater Discharge Area using Satellite image around Jeju. *The Journal of the Korea institute of electronic communication sciences*, 7(2), 439-441.

Peterson, R. N., Burnett, W. C., Glenn, C. R., & Johnson, A. G. (2009). Quantification of point-source groundwater discharges to the ocean from the shoreline of the Big Island, Hawaii. *Limnology and Oceanography*, 54(3), 890-904.

Redjimi, A., Knežević, D., Savić, K., Jovanović, N., Simović, M., & Vasiljević, D. (2014). Noise equivalent temperature difference model for

thermal imagers, calculation and analysis. *Scientific Technical Review*, 64(2), 42-49.

Tamborski, J. J., Rogers, A. D., Bokuniewicz, H. J., Cochran, J. K., & Young, C. R. (2015). Identification and quantification of diffuse fresh submarine groundwater discharge via airborne thermal infrared remote sensing. *Remote Sensing of Environment*, 171, 202-217.

Tcherepanov, E. N., Zlotnik, V. A., & Henebry, G. M. (2005). Using Landsat thermal imagery and GIS for identification of groundwater discharge into shallow groundwater-dominated lakes. *International Journal of Remote Sensing*, 26(17), 3649-3661.

United States Geological Survey (2013). Product Guide: Landsat Climate Data Record (CDR). Surface Reflectance; Version 5.3; Department of the Interior U.S. Geological Survey: Washinton, DC, USA, December 2013.

Varma, S., Turner, J., & Underschultz, J. (2010). Estimation of submarine groundwater discharge into Geographe Bay, Bunbury, Western Australia. *Journal of Geochemical Exploration*, 106, 197–210.

Vogelmann, J. E., Xian, G., Homer, C., & Tolk, B. (2012). Monitoring gradual ecosystem change using Landsat time series analyses: Case studies in selected forest and rangeland ecosystems. *Remote Sensing of*

Environment, 122, 92-105.

Wang, L. T., McKenna, T. E., & Deliberty, T. L. (2008). Report of Investigations No. 74: Locating ground-water discharge areas in Rehoboth and Indian River Bays and Indian River Delaware using Landsat 7 imagery. Newark, State of Delaware: Delaware Geological Survey.

Wilson, J., & Rocha, C. (2012). Regional scale assessment of Submarine Groundwater Discharge in Ireland combining medium resolution satellite imagery and geochemical tracing techniques. *Remote Sensing of Environment*, 119, 21-34.

Xing, Q., Braga, F., Tosi, L., Lou, M., Wu, L., Tang, C., ... & Teatini, P. (2014). Towards detecting fresh submarine groundwater discharge at the Laizhou Bay (Southern Bohai Sea, China) by remote sensing methods.

국문 요약

최근 들어 여러 학자들이 해저 지하수 유출에 높은 관심을 보이고 있으며, 많은 연구가 활발히 진행되고 있다. 그러나 아직 밝혀지지 않은 해저 지하수 유출이 많이 존재한다. 해저 지하수 유출은 시간과 장소에 따라 다른 형상으로 나타나기 때문에 다중 시기의 자료가 해저 지하수 유출 신호를 탐지하는데 유용한 자료가 될 수 있다. 다중 시기의 자료는 시, 공간에 따라 다르게 나타나는 해저 지하수 유출 신호 탐지에 효과적일 뿐 아니라 약한 해저 지하수 유출 신호를 탐지하는 데에도 도움이 된다. 또한, 이러한 해저 지하수 유출의 시간과 공간에 따라 다르게 나타나는 변화성과 장소에 따라 유출되는 세기의 다양성 때문에 한 장의 위성영상으로 해저 지하수 유출을 탐지하기에는 다소 어려움이 있다. 따라서 본 연구에서는 지금까지 해저 지하수 유출 탐지에 사용된 적 없는 Landsat 자료를 이용한 stacking 방법을 제시한다. 또한, 이 방법은 노이즈(noise)와 구분하기 어렵거나 매우 약한 해저 지하수 유출 신호를 탐지하는데 매우 효과적이고 의미 있는 방법이다.

Stacking 방법은 크게 다음의 2가지 과정으로 진행된다. 먼저, 해저 지하수 온도가 포함되지 않은 평균 해수면온도로부터 해저 지하수 온도편차를 계산한다. 다음으로 월(月)과 조수 조건을 분석한 후, 해저 지하수 온도편차 데이터들을 월과 조수 조건에 따라 중첩하여 해저 지하수 유출이 존재함을 확인한다. 최적의 중첩 조건을 고려한 stacking 방법을 통해 제주도의 세 곳의 연구지역에서 해저 지하수 유출 신호를 확인하였다. 또한, 본 연구는 한 장의 위성영상으로는 확인하기 어려운

신호가 약한 해저 지하수 유출 신호도 stacking 방법을 통해 위성영상으로 탐지 가능함을 증명하였다. 또한, 노이즈와 구분하기 어려운 불분명한 해저 지하수 유출신호를 찾아내는데 유용한 방법임을 확인하였다.

본 연구에서 사용된 평균 해저 지하수와 해수면의 온도는 제주도에 해당하는 값으로, 관심지역의 평균 해저 지하수와 해수면의 온도를 적용한다면 이 방법을 통해 세기가 약한 해저 지하수 유출신호를 탐지할 수 있을 것이라고 판단된다.